Broadband 400 GHz On-Chip Antenna With a Metastructured Ground Plane and Dielectric Resonator

Bersant Gashi, Dominik Meier, Laurenz John, Benjamin Baumann, Markus Rösch, Axel Tessmann, Arnulf Leuther, and Rüdiger Quay, *Senior Member, IEEE*

***Abstract*— The analysis, modeling, design, simulation, and experimental evaluation of a 400 GHz on-chip antenna is presented, with a novel combination of metastructures, a microstrip patch, a quartz-based dielectric resonator, and a diamond-based antireflex layer—all integrated on a 35 nm InGaAs metamorphic high-electron-mobility transistor (mHEMT) technology. The said combination represents a first-time implementation for all submillimeter-wave-capable semiconductor technologies. Circumventing a substrate-thickness limitation of 4.98 μm, a state-of-the-art broadband, efficient, and to-the-broadside radiating on-chip antenna solution is realized. It achieves a measured impedance bandwidth of 100 GHz, 25.6%, spanning from 340 to 440 GHz. A consistent pattern bandwidth of 75 GHz is recorded, with an efficiency of 50%–66% and a directivity of up to 10.4 dBi—or 27 dBi, with the utilization of a polypropylene-based dielectric lens. The theoretical analysis of the proposed on-chip antenna is presented, and two modeling approaches are shown and compared. Between the analytical and the 3-D electromagnetic (EM) model, the latter is chosen as it offers greater precision in defining the metastructure unit cell and enables the inclusion of the remaining components of the proposed antenna setup. The measured reflection coefficient and far-field patterns are compared to simulations via the utilized model, and a strong agreement is observed. These far-field patterns are acquired with the on-chip antenna inserted within a broadband 400 GHz transmitter submillimeter-wave monolithic integrated circuit, processed on the 35 nm mHEMT technology.**

***Index Terms*— Dielectric resonator, metamorphic high-electron-mobility transistor (mHEMT), metastructures, on-chip antenna, transmitter.**

Manuscript received 25 June 2021; revised 4 May 2022; accepted 9 May 2022. Date of publication 30 May 2022; date of current version 9 November 2022. This work was supported by the German Federal Ministry of Defence (BMVg) and the Bundeswehr Technical Center for Information Technology and Electronics (WTD81) in the framework of the RADKOM Program. *(Corresponding author: Bersant Gashi.)*

Bersant Gashi, Laurenz John, Benjamin Baumann, Axel Tessmann, Arnulf Leuther, and Rüdiger Quay are with the Fraunhofer Institute for Applied Solid State Physics (IAF), 79108 Freiburg im Breisgau, Germany (e-mail: bersant.gashi@iaf.fraunhofer.de).

Dominik Meier was with the Fraunhofer Institute for Applied Solid State Physics (IAF), 79108 Freiburg im Breisgau, Germany. He is now with AP Sensing GmbH, 71034 Böblingen, Germany.

Markus Rösch was with the Fraunhofer Institute for Applied Solid State Physics (IAF), 79108 Freiburg im Breisgau, Germany. He is now with Dolphin Design SAS, 38240 Meylan, France.

Color versions of one or more figures in this article are available at https://doi.org/10.1109/TAP.2022.3177527.

Digital Object Identifier 10.1109/TAP.2022.3177527

I. Introduction

SUBMILLIMETER-WAVE frequency bands allow for broadband transmit and receive windows, serviceable to both communications [1]–[5] and radar-based [6]–[15] applications—increasing data rates and imaging resolutions, respectively. The submillimeter-wave operational frequency allows for miniaturized integrated-circuit (IC) elements. This promotes singular-chip solutions, which integrate complete active chains with the corresponding on-chip antennas. A majority of such fully integrated solutions are based on state-of-the-art silicon-on-insulator (SOI) complementary metal–oxide–semiconductor (CMOS) and SiGe bipolar CMOS (BiCMOS) technology nodes [16]–[26]. While there is a benefit in the available dielectric thickness in the back-end-of-line (BEOL) of SOI CMOS and SiGe BiCMOS, the corresponding maximum oscillation frequency restricts applications in terms of the realizable bandwidth [27]. Fraunhofer IAF's 35 nm $In_{0.52}Al_{0.48}As/In_{0.80}Ga_{0.20}As$ metamorphic high-electron-mobility transistor (mHEMT) IC technology boasts a transition and maximum oscillation frequency of $f_T > 500$ GHz and $f_{max} > 1000$ GHz [28], [29]. Processed on the said technology, complete active chains are capable of supporting a relative bandwidth of up to 30% [30]–[33]. Yet, a major drawback for realizing broadband and to-the-broadside radiating on-chip antennas is the limiting thickness of the combined benzocyclobutene (BCB) dielectric layers, as shown in Fig. 1 to be 4.98 μm. The latter is defined between the ground plane, metal layer MET1, and the top metal layer METG. Henceforth, the term "substrate" is used to define the combination of BCB3, SiN, and BCB2. Regarding a center frequency (f_c) of 400 GHz, the ratio between the substrate thickness and the nominal wavelength h/λ_0 is below 0.006. This restricts a microstrip patch antenna approach to a relative bandwidth of below 4%. In this regard, the on-chip microstrip antenna can be viewed as a lossy capacitor [34].

The intent of this article is to present an efficient, broadband, and to-the-broadside radiating on-chip antenna for substrate-limited submillimeter-wave-capable semiconductor technologies. In order to achieve the said goal, the first-time combination of metastructures, a dielectric resonator, an antireflex layer, and a microstrip patch antenna is presented. These are all unified in a broadband transmitter submillimeter-wave monolithic integrated circuit (S-MMIC), processed on the

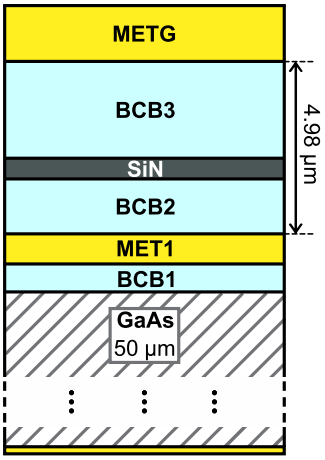

Fig. 1. 35 nm mHEMT on-chip antenna BEOL.

aforementioned 35 nm mHEMT technology. No alteration in the BEOL is required. The restricted substrate thickness is electrically elongated via the utilization of a metastructured ground plane. The reflected substrate-incident waves are utilized to excite standing waves in the quartz-based dielectric resonator positioned on top. The efficient decoupling of the resulting standing waves is achieved via the addition of a thin antireflex diamond layer. The S-MMIC is assembled on a submount carrier board and a laser-sintered polypropylene-based dielectric lens is included. The mentioned components are designed for operation in the WR-2.2 waveguide frequency band (325–500 GHz).

Submillimeter-wave approaches that share similarities with the presented on-chip antenna solution can be found in the following:

1) [35], where dielectric resonators are paired with a substrate-integrated waveguide cavity-backed on-chip antenna processed in SiGe BiCMOS;
2) [36], where a metastructure-based antenna array is realized on a GaAs substrate. The array is fed by through-the-substrate vias connecting to slot lines processed on the backside;
3) [37], where a dielectric resonator is combined with a microstrip patch processed in SOI CMOS;
4) [38], where a metastructure-based antenna array is realized in SOI CMOS. The radiating elements are fed from the backside of the wafer via a combination of slot lines and open-circuited stubs;
5) [16], where a thin superstrate is combined with a 1-D microstrip-antenna-based phased array processed in SOI CMOS.

The unique difference between the aforementioned and this work lies in the utilization of a metastructured ground plane as an artificial magnetic conductor that reflects the substrate-incident waves and excites multiple modes within a quartz-based dielectric resonator. Not only is the bandwidth addressed, rather the coapplication contributes toward consistent radiation patterns.

This article is divided into four further sections, excluding the introduction. Section II contains the theoretical analysis, modeling, and simulation of the proposed antenna solution.

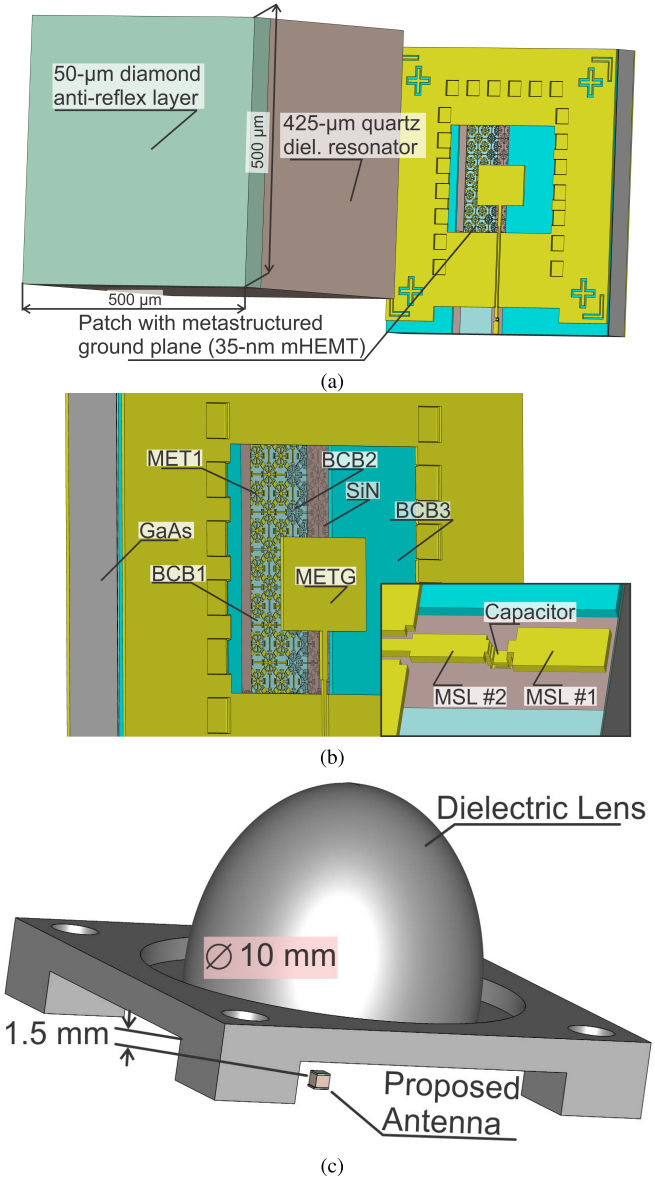

Fig. 2. (a) 3-D EM model of the complete on-chip antenna implementation, (b) respective realization of the mHEMT stack as well as the input-matching network, and (c) the included dielectric lens.

Sections III and IV focus on the characterization and interpretation of the reflection coefficient (S_{11}) and far-field patterns, respectively. Measurements and simulations are included and scrutinized. Finally, a brief conclusion is provided in Section V.

II. On-Chip Antenna

The 3-D electromagnetic (EM) model of the proposed on-chip antenna solution is shown in Fig. 2(a). It consists of the metastructured ground plane and microstrip patch, both processed in the mHEMT stack. The quartz dielectric resonator and diamond antireflex layer are included as well. The design environment is that of CST Studio Suite (CST). A closer look of the metastructure and patch is shown in Fig. 2(b), where the BEOL of the utilized process is reflected. The input-matching network, composed of an

inductor–capacitor–inductor arrangement, is highlighted as well. It makes use of the SiN layer to implement the desired parallel capacitance. This "lumped" approach is more compact than a microstrip-line-based radial stub. It induces less losses and allows for direct integration with the active chain.

The implemented antenna concept includes a polypropylene-based dielectric elliptical lens, which is shown in Fig. 2(c). The parametric values utilized in the design process in terms of the dielectric permittivity (ϵ_r) and loss tangent (tan δ) are 2.2 and 0.00055, respectively [39]. The lens has a diameter of 10 mm and an offset to the phase center of the dielectric resonator of 1.5 mm. The latter is acquired via EM simulation.

Each component of the proposed on-chip antenna is individually discussed in the following subsections. The analytical and the EM modeling of the metastructure and dielectric resonator are presented.

A. Metastructures

The utilization of metastructures in tandem with planar antennas is discussed prior in [40]–[42]. These are predominantly deployed to suppress surface currents via the synthesis of bandgap-material-like properties. The modeling methods utilized in this work are an adaptation of what is initially presented in [43], adjusted to fit the 35 nm mHEMT stack.

The metastructured ground plane allows for a controlled reflection of the substrate-incident waves, where the resulting phase delay is within a range from $-90°$ to $90°$. The phase reference point is set at the top metal layer METG located 4.98 μm above MET1. Within the operating bandwidth—the frequency span in which the aforementioned phase delay is present—the reflected substrate-incident waves and the radiated waves undergo constructive interference. Furthermore, the metastructured ground plane presents a high surface impedance. This ensures that the percentile of the substrate-incident waves entering the 50 μm GaAs substrate is as low as possible. As such, through the utilization of metastructures, a high-impedance ground plane is realized with artificial magnetic conductor properties—despite a large electric field along the surface, the tangential magnetic field is small. This implementation increases the bandwidth and radiation efficiency within the operating frequency. It improves the far-field patterns of the complete setup as well [41], [42].

The metastructure unit cell represents a defined repeating pattern with its unit dimensions below a tenth of the operating wavelength. For this work, the pattern of choice is presented in Fig. 3. The design makes use of a uniplanar metastructure surface, with its unit cells resembling heavily altered Jerusalem-cross-like structures. The latter are expanded upon with additional axes every 45°, allowing for a wider range of incidence angles for the in-substrate waves. Furthermore, the gaps between these structures are filled with singular segments that alternate in their vertical and horizontal orientations. These provide a further resonance and allow for a denser metastructure layout. The implemented metastructure omits the usage of through-substrate vias and takes into consideration co-polarization and cross polarization. The desired inductance is obtained from the current loop along

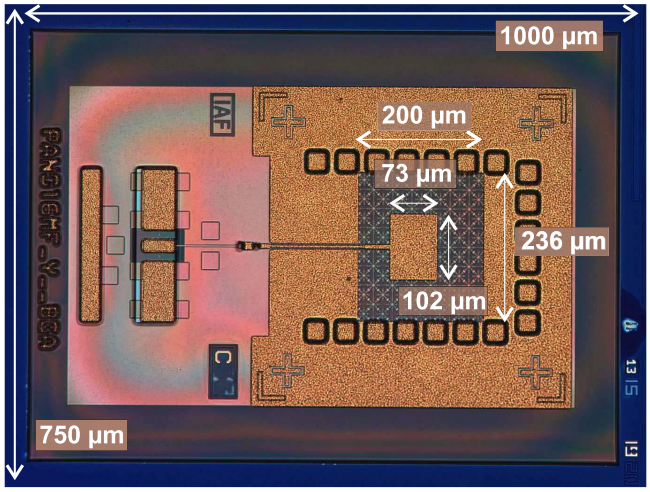

(a)

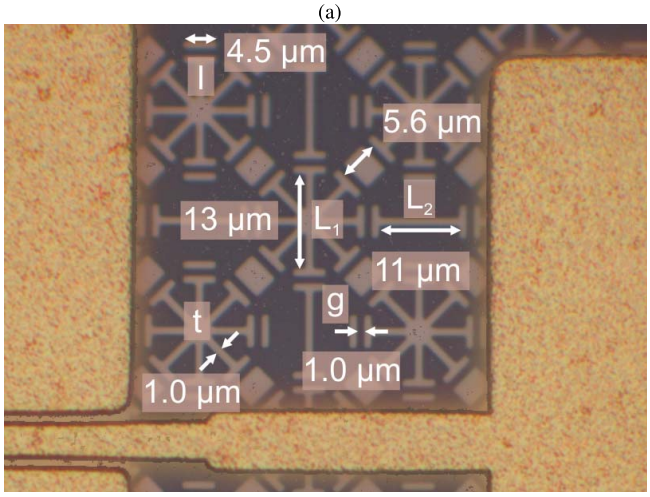

(b)

Fig. 3. (a) Microphotograph of the fabricated stand-alone on-chip antenna. (b) Zoomed-in image of the metastructured ground plane sitting 4.98 μm below METG.

the length of the segments and axes, while the capacitance is derived from the gap and edge length between two adjacent metallic structures. The unit cell as a whole is symmetric. The dimensions of the microstrip patch and metastructure unit cell are included in Fig. 3—the patch is discussed later in the text. The processed stand-alone on-chip antenna can be seen in Fig. 3(a). It contains the respective radio frequency (RF) pad and extension for RF-probing. A close view of the processed metastructure, 4.98 μm below the top metal, can be seen in Fig. 3(b). The capacitive portion is composed of an edge length of 4.5 μm and a gap width of 1 μm. The inductive portion is composed of either an axis length of 13 or 11 μm. The uniform thickness of all the segments is 1 μm.

Such a metastructure can be approximated via the application of the loaded transmission-line model for plane-wave incidences, as initially established in [44] and [43] and highlighted in [42]. This analytical model is altered and adjusted specifically for the 35 nm mHEMT technology. A graphical interpretation is presented in Fig. 4. The main idea lies in the evaluation of the phase of the reflection coefficient for which the complex surface impedance of the metastructured

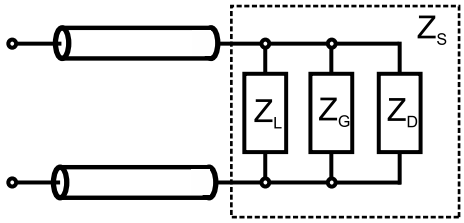

Fig. 4. Loaded transmission-line model for plane-wave incidences in the utilized 35 nm mHEMT technology.

ground is required. The evaluation of the latter is achieved via the separation of the model into a frequency-selective surface with an impedance Z_G, the respective transition from the reference height of 4.98 μm to the metastructured layer with an impedance Z_L, and the transition from the latter to the ground plane with an impedance Z_D. The resulting metastructure surface impedance Z_S and the respective reflection coefficient for both transverse electric (TE) and transverse magnetic (TM) waves are

$$Z_S = \left(\frac{Z_G Z_D + Z_L Z_D + Z_L Z_G}{Z_L Z_G Z_D}\right)^{-1} \tag{1}$$

$$\Gamma^{TE} = \frac{Z_S - \eta_L \cos^2\theta_{in}}{Z_S + \eta_L \cos^2\theta_{in}} \tag{2}$$

$$\Gamma^{TM} = \frac{Z_S \cos^2\theta_{in} - \eta_L}{Z_S \cos^2\theta_{in} + \eta_L}. \tag{3}$$

The incident plane wave originates from the microstrip patch in the METG layer, and thus, the formulation slightly deviates from what is presented in [43]. The wave impedance η_L does not refer to free space, but rather to the impedance seen in the medium created through the combination of the BCB3, SiN, and the BCB2 layers. The angle of incidence is denoted by θ_{in}. At the resonance angular frequency ω_0, the following holds true [42], [43]:

$$\mathrm{Im}(Z_L(\omega_0)) + \mathrm{Im}(Z_G(\omega_0)) + \mathrm{Im}(Z_D(\omega_0)) = 0. \tag{4}$$

Considering the influence of the mHEMT stack and the geometry of the unit cell, the respective TE and TM complex impedances of the three main layers can be approximated as follows [43]:

$$Z_D^{TE} \approx j\omega\mu_{(\mathrm{GaAs,\ BCB1})} h_{(\mathrm{GaAs,\ BCB1})} \tag{5}$$

$$Z_L^{TE} \approx j\omega\mu_{(\mathrm{BCB3,\ SiN,\ BCB2})} h_{(\mathrm{BCB3,\ SiN,\ BCB2})} \tag{6}$$

$$Z_D^{TM} \approx j\omega\mu_{(\mathrm{GaAs,\ BCB1})} h_{(\mathrm{GaAs,\ BCB1})} \cos^2\theta_{in} \tag{7}$$

$$Z_L^{TM} \approx j\omega\mu_{(\mathrm{BCB3,\ SiN,\ BCB2})} h_{(\mathrm{BCB3,\ SiN,\ BCB2})} \cos^2\theta_{in} \tag{8}$$

$$Z_G^{TE} = Z_G(\omega, L_G, C_G) = j\omega L_G + \frac{1}{j\omega C_G} \tag{9}$$

$$Z_G^{TM} = Z_G(\omega, L_G, C_G)\cos^2\theta_{in}. \tag{10}$$

In the above, the relative permeability—dependent on which portion of the mHEMT stack is considered either $\mu_{(\mathrm{BCB3,\ SiN,\ BCB2})}$ or $\mu_{(\mathrm{GaAs,\ BCB1})}$—can be expressed as a product of the relative permittivity (dielectric constant) and the square of the relative wave impedance, $\mu_L = \epsilon_L \eta_L^2$. These parameters are acquired via an EM simulation of the 35 nm mHEMT stack. Dependent on which portion of the stack is considered, the height h varies between 4.98 and 51.4 μm. Equations (9) and (10), are dependent on the shape of the metastructure unit cell, thus the effective capacitance C_G—originating from the capacitive coupling of adjacent structures—and effective inductance L_G—originating from the surface currents on the straight portions of the repeating unit cell. The following equations represent slight alterations to what can be found in [43] for expressing L_G and C_G of these heavily altered Jerusalem-star-like structures:

$$L_G = \frac{\eta'}{2\omega}(\alpha_1 + \alpha_2) \tag{11}$$

$$\alpha_1 = \frac{k' L_1}{\pi}\ln\left(\frac{4L_1}{\pi t}\right) \tag{12}$$

$$\alpha_2 = \frac{k' L_2}{\pi}\ln\left(\frac{L_2}{\pi t}\right) \tag{13}$$

where η' is the wave impedance of the effective medium (GaAs and BCB1), which is extracted via an EM simulation of the 35 nm mHEMT stack. α_1 and α_2 are the grid parameters for the expanded Jerusalem-star-like structure and the alternating segments. L_1, L_2, and t denote the dimensions of the unit cell and can be found in Fig. 3(b). k' is the wavenumber of the effective medium and is expressed as follows [43]:

$$k' = \omega\sqrt{\epsilon_L \mu_L \frac{(\epsilon_D + 1)}{2}}. \tag{14}$$

The effective capacitance is expressed as [43]

$$C_G = \frac{2}{\pi}\epsilon_D \epsilon_L l\left[\ln\left(\mathrm{cosec}\left(\frac{\pi g}{4L_1}\right)\right) + F\right] \tag{15}$$

$$F = \frac{Qu^2}{1 + Q(1-u)^2} + \left(\frac{lu(3u-2)}{4\lambda'}\right)^2 \tag{16}$$

where $\lambda' = 2\pi/k'$ is the wavelength of the effective medium [43]

$$Q = \sqrt{1 - \left(\frac{l}{\lambda'}\right)^2} \tag{17}$$

$$u = \cos^2\left(\frac{\pi g}{2l}\right). \tag{18}$$

l and g represent the dimensions of the metastructure, which can be found in Fig. 3(b).

These analytical formulations provide an understanding as to what affects the total impedance Z_S, thus the reflection coefficient. As aforementioned, the dielectric properties of the respective layers are extracted via an EM simulation of the 35 nm mHEMT stack. Due to the difficulties in characterizing such a multilayer stack at the operating frequency of 400 GHz, a dependency on EM-simulated results is present. Taking into consideration that the proposed antenna includes a microstrip patch, a dielectric resonator, and an antireflex layer, a full 3-D EM numerical simulation approach via CST is chosen in favor of the analytical model. The resulting phase responses of both approaches are discussed in the next paragraph. A 3-D EM model of the unit cell, including periodic boundaries and a plane-wave source, is shown in Fig. 5(a). The model contains the complete BEOL, partially concealed for an improved

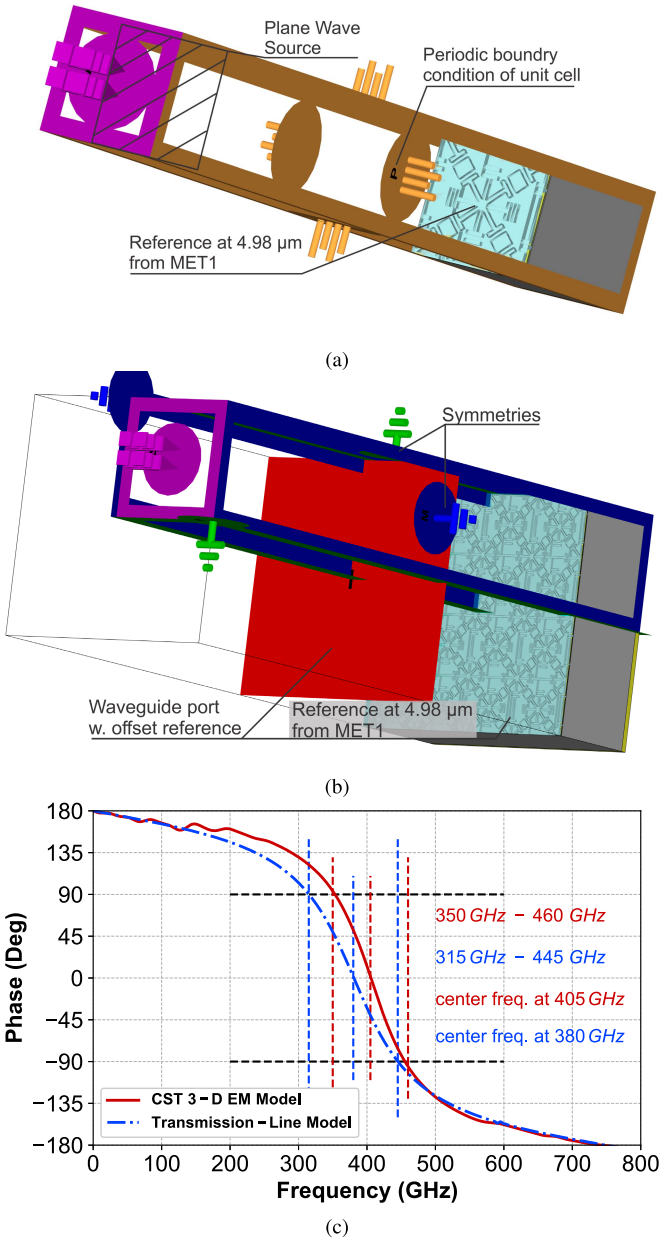

Fig. 5. (a) Metastructure unit cell plane-wave-based 3-D EM model. (b) Complete waveguide-based 3-D EM model. (c) The unwrapped phase of the reflected substrate-incident waves at the desired reference offset of 4.98 μm. Data are acquired via both the analytical and 3-D EM models.

visual recognition. A field probe is placed 4.98 μm from the metastructured layer, and the phase of the reflected signal is analyzed. Since the periodic boundaries ensure an infinitely expanding and repeating structure, a feature that is not found in practice, a larger segment of the metastructure is simulated via a waveguide excitation port and respective symmetry boundaries, as presented in Fig. 5(b).

The unwrapped phase response of the reflected signal can be viewed in Fig. 5(c). It is acquired via both the analytical (transmission-line) model and the 3-D EM model. A normal incidence angle is selected for θ_{in}. Since the metastructure is symmetric, only the TE case is plotted. With regard to the EM simulation, the desired phase shift from $-90°$ to $90°$ is present within a range of 350–460 GHz. Compared to the transmission-line model, the anticipated range is from 315 to 445 GHz. The center frequency acquired via the transmission-line model is at 380 GHz. The center frequency of the 3-D EM model is at 405 GHz. The deviation of 20 GHz in the operating bandwidth and a 35 GHz offset in the center frequency is due to the accurateness of the adapted transmission-line model. It is highly dependent on the approximation of the complexity of the unit cell and the technology stack. The need for a large operating bandwidth dictates the usage of more involved structures, which due to the high operating frequency have a miniature size. Nonetheless, once the dielectric properties of the respective layers are a known quantity, the analytical model allows for a more computing time-efficient manner of estimating the phase response. The presented results indicated an operating bandwidth of 110 GHz. This allows for an efficient, broadband, and to-the-broadside radiating on-chip antenna to be realized in the 35 nm mHEMT technology, as at least half of the reflected substrate-incident waves undergo a constructive interference with the radiated and evanescent ones.

The respective experimental validation is performed as part of the complete antenna setup. Individually characterizing such a layer is impossible, due to the miniature distances that have to be considered in a transmission-and-reflection measurement. Rather, the characterization is performed as part of the reflection-coefficient and far-field measurements of the complete antenna solution.

B. Dielectric Resonator and Antireflex Layer

The metastructured ground plane allows for the virtual elongation of the substrate height resulting in an increased impedance bandwidth. However, the combined effect of it and a quartz dielectric resonator is required to increase the pattern bandwidth. Making use of the microstrip patch on METG as a feeding point, the 3-D EM model is extended to contain a quartz rectangular resonator. As highlighted in Fig. 3(a), the microstrip patch has an edge length of 73 μm and a corresponding width of 102 μm. These dimensions differ from what is expected by standard formulations [45], due to the influence of the multilayer stack, the quartz on top, and the metastructure underneath. Since the latter is not a perfect magnetic conductor, the GaAs substrate is partially opened. Thus, it influences the final dimensions of the patch. In such a use case, the implementation of a 3-D EM simulation is essential in designing the microstrip patch.

As can be seen in Fig. 3(a), the microstrip patch has a grounded frame connected through vias to the backside metal. The resonator functions if a strong magnetic field is excited on a dielectric slab placed on top of a grounded plane. The frame around the microstrip patch represents the latter. The distance of this frame to the edges of the microstrip patch is approximately a quarter wave in the respective dielectric medium—namely, an edge length of 200 μm and width of 236 μm, optimized via an EM simulation. This allows for the reflected surface currents to be in-phase with the fringing fields.

With regard to the dielectric resonator, charged particles passing through the microstrip patch-induced magnetic

field cause fringing fields. Reflections from its sidewalls induce standing waves and store electrical energy. The various resonant modes, or field states, that persist within its semi-permeable dielectric walls define the surface-current density distributions and, thus, the radiation patterns. The aforementioned effect of the metastructured ground plane to reduce unwanted and sporadic surface currents inherently supports this particular type of integration and contributes toward pattern stability. Furthermore, the transition from the BCB3 to the quartz is advantageous for the EM waves.

The mode propagation within the dielectric resonator depends mainly on its dimensions, relative permittivity, and point of excitation [46]. In this work, quartz was selected as the desired material with a permittivity (ϵ_{r-SiO_2}) of 3.75. It represents a favorable transition from BCB3, which has a permittivity ($\epsilon_{r\text{-}BCB3}$) of 3.2. Due to mechanical restrictions (as of the writing of this article), the lateral dimensions of the quartz slab are fixed to 500 μm. The point of excitation is chosen to be the center of the slab's side making contact with the BEOL since it yields a uniform field distribution. The remaining variable is the vertical z-dimension. Under the assumption of perfect-electrical-conductor boundaries on the four sides of the rectangular slab, with perfect-magnetic-boundary conditions on the bottom and top, the resonant frequency is given by [46]

$$f_r = \frac{c}{2\pi\sqrt{\epsilon_{r\text{-}SiO_2}\mu_{r\text{-}SiO_2}}}\sqrt{\left(\frac{z_1\pi}{a}\right)^2+\left(\frac{z_2\pi}{b}\right)^2+\left(\frac{z_3\pi}{d}\right)^2} \tag{19}$$

where z_1, z_2, and z_3 are integers, while a, b, and d are the dimensions of the rectangular slab.

With regard to the height d, (19) is utilized to define an initial starting point for the design process. It is in the range of 375–475 μm. Since the boundary conditions required for (19) are not present in the implemented design, a full 3-D EM simulation and accompanying parameterized sweep is required. The final dielectric slab height of 425 μm is chosen as it results in the desired far-field response. Furthermore, it retains a height-to-lateral-dimensions ratio compatible for mechanical dicing and excites the $TE_{\delta,1,4}$ mode—as shown Fig. 6(a). The far-field pattern at 400 GHz, which results due to the modes induced in the dielectric resonator, is shown in Fig. 6(b). A simulated realized gain of 7.8 dBi is present. The radiation direction is to the broadside.

To improve the decoupling of the wave in the propagating z-direction, an antireflex layer is added to the top of the dielectric resonator. This layer comes in the form of a $500\times 500\times 50$ μm^3 polycrystaline diamond piece with a permittivity ($\epsilon_{r\text{-}C}$) of 5.68. The EM waves are pulled toward the diamond plate, which is sufficiently thin as to not induce standing waves, thus effectively decoupling the EM waves toward free space. A high-frequency capable, thin dielectric material with a respective dielectric constant between the values of 5 and 6, deduced from EM simulations, is desired. A material with a higher ϵ_r may result in a mismatched transition and, thus, in the reflection of the EM waves and subsequent hampering of the metastructured layer.

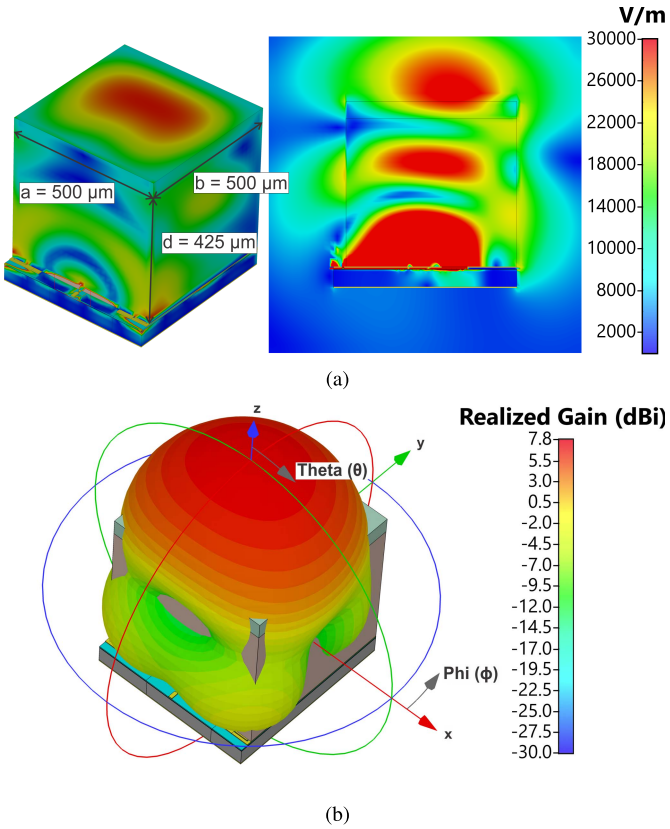

Fig. 6. (a) Simulated E-field of the 3-D EM model in CST at 400 GHz (left) and the respective $TE_{\delta,1,4}$ mode (right). (b) Far-field pattern at 400 GHz, as a result of the propagating modes.

III. Reflection-Coefficient Characterization

In order to characterize the reflection coefficient of the proposed antenna, a stand-alone variant is processed, as shown in Fig. 7(a). It contains the required RF-contacting pad and microstrip-line extension. To the left, the processed chip is presented with the quartz dielectric resonator on top. To the right, the additional antireflex diamond layer is added on top and the side view of the complete setup can be seen.

Fig. 7(b) presents the measured and simulated S_{11}. The measurements are acquired via an Agilent N5224A PNA network analyzer in combination with a Virginia Diodes, Inc. WR-2.2 extension. The utilized T-Wave T500 RF-probe is calibrated via a through-reflect-line procedure on a standard-impedance substrate. The plotted results do not include the dielectric lens.

The measured impedance bandwidth spans from 340 to 440 GHz or a 25.6% relative bandwidth. The simulations consist of multiple curves, namely, the initial design, which ignores any BEOL deformations of the mHEMT process. The simulated impedance bandwidth of this initial design spans from 330 to 460 GHz. The second iteration, labeled "True-to-Processed-BEOL," updates the EM model to include the overgrowth of the METG layer and the shrinking of the capacitor-contacting via since these systematic deviations from the designed sizes were not considered in the initial model. The simulated impedance bandwidth ranges from 340 to 425 GHz. The third iteration, labeled "true-to-processed-BEOL and RF-pad compensation," considers the

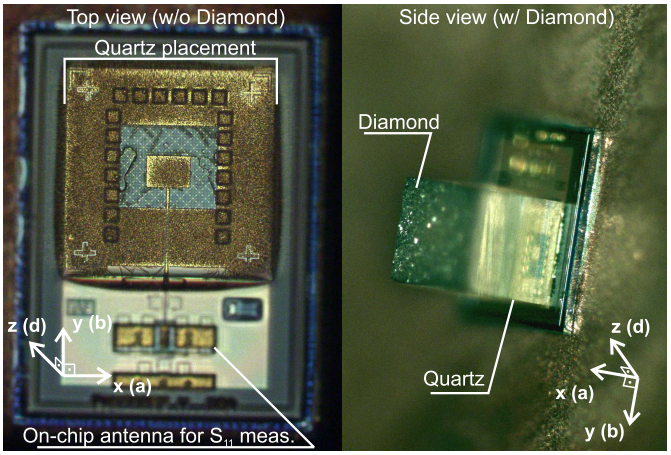

(a)

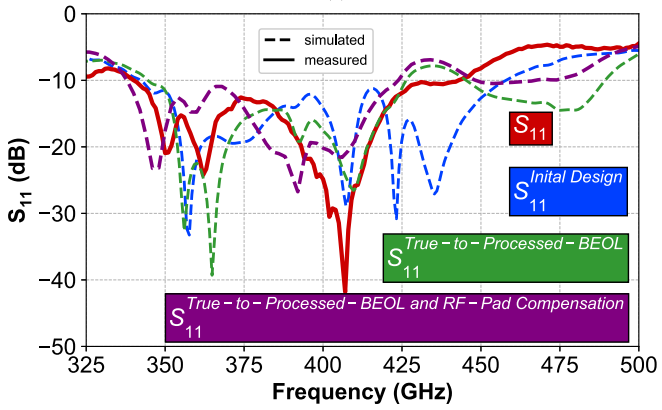

(b)

Fig. 7. (a) Fabricated on-chip antenna: quartz placement (left), a tilted view of the diamond and quartz (right). (b) S_{11} characterization of the complete on-chip antenna, plotted versus the simulation.

influence of the RF-pad and microstrip-line extension. The EM model is updated accordingly. The simulated impedance bandwidth ranges from 330 to 425 GHz. The resonance peaks and overall behavior across the operating bandwidth fit well with the measurement.

In order to gain a better understanding of the measured relative bandwidth of 25.6%, the proposed solution is compared to a hypothetical microstrip patch antenna implementation within an "ideal" BEOL that supports a BCB-substrate thickness of 105 μm. This would ensure that the reflected substrate-incident waves are in-phase with the radiated ones. Such a dielectric thickness within the BEOL of the 35 nm process is beyond any realm of possibility. Nonetheless, it presents a good comparison to reveal the advancements made with the coapplication of the metastructured ground plane and dielectric resonator.

To calculate the relative impedance bandwidth of this hypothetical "ideal" solution, the radiated power from the fringing fields P_{Rad} and the surface-wave power P_{SW} must be considered, yielding a bandwidth formulation as follows [47]:

$$\text{BW} = \frac{16 C_1 h_{\text{ideal}} p W_{\text{P}}}{3\sqrt{2}\eta_{\text{SW}} \epsilon_{\text{r-BCB}} \lambda_0 L_{\text{P}}} \tag{20}$$

$$C_1 = 1 - \frac{1}{\epsilon_{\text{r-BCB}}} + \frac{0.4}{\epsilon_{\text{r-BCB}}^2} \tag{21}$$

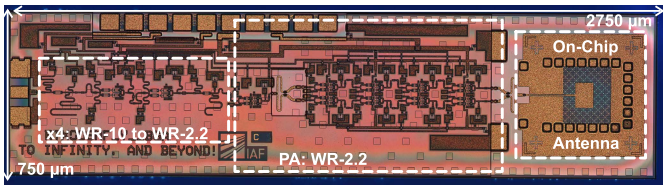

Fig. 8. Microphotograph of the fabricated transmitter S-MMIC with the proposed on-chip antenna.

with $\epsilon_{\text{r-BCB}}$ denoting the dielectric constant of the "ideal" BCB substrate with a height of $h_{\text{ideal}} = 105$ μm. The surface-wave radiation efficiency η_{SW} is [47]

$$\eta_{\text{SW}} = \frac{P_{\text{Rad}}}{P_{\text{Rad}} + P_{\text{SW}}} = \frac{4C_1}{4C_1 + 3\pi k h_{\text{ideal}} \mu_{\text{r-BCB}} (1 - 1/\epsilon_{\text{r-BCB}})^3}. \tag{22}$$

Considering the ratio between the radiated power from a rectangular patch and that of a Hertzian dipole, as well as the patch length L_{P}, the width W_{P} and the propagation constant $k = 2\pi/\lambda_0$ [47]

$$p = 1 - \frac{0.16605(kW_{\text{P}})^2}{20} + \frac{0.02283(kW_{\text{P}})^4}{560} - \frac{0.09142(kL_{\text{P}})^2}{10}. \tag{23}$$

To utilize (20), L_{P} and W_{P} are required. These can be found via models that rely on radiating fringing fields, which extend the effective electrical size of the microstrip patch by Δ [48]

$$\Delta = 0.412h \frac{\epsilon_{\text{eff-BCB}} + 0.3}{\epsilon_{\text{eff-BCB}} - 0.258} \frac{W_{\text{P}}/h_{\text{ideal}} + 0.262}{W_{\text{P}}/h_{\text{ideal}} + 0.813} \tag{24}$$

where $\epsilon_{\text{eff-BCB}}$ is the effective dielectric constant [49]

$$\epsilon_{\text{eff-BCB}} = \frac{\epsilon_{\text{r-BCB}} + 1}{2} + \frac{\epsilon_{\text{r-BCB}} - 1}{2}\left(1 + \frac{10h_{\text{ideal}}}{W_{\text{P}}}\right)^{-1/2} \tag{25}$$

for which the patch width is defined as

$$W_{\text{P}} = \frac{c_0}{2f_0\sqrt{\epsilon_{\text{r-BCB}}}}. \tag{26}$$

Knowing (24)–(26), the patch length can be devised by

$$L_{\text{P}} = \frac{c_0}{2f_0\sqrt{\epsilon_{\text{eff-BCB}}}} - 2\Delta. \tag{27}$$

Calculating the required parameters via (21)–(27) allows for the relative impedance bandwidth of the hypothetical microstrip patch antenna to be calculated via the usage of (20), yielding a BW = 31.5%. Since the actual substrate thickness is only 4.98 μm, a factor of 21 smaller than the "ideal" case, the achieved value of 25.6%, when compared to the hypothetical, shows how successful the presented metastructure-and-dielectric-resonator combination truly is.

IV. Far-Field Characterization

Due to the miniature size of the on-chip antenna, the direct RF-probing of it introduces a much larger metallic object within the near-field region. This degrades the far-field patterns and makes such a characterization impossible. Thus, in order to solve the said issue, the proposed antenna is integrated

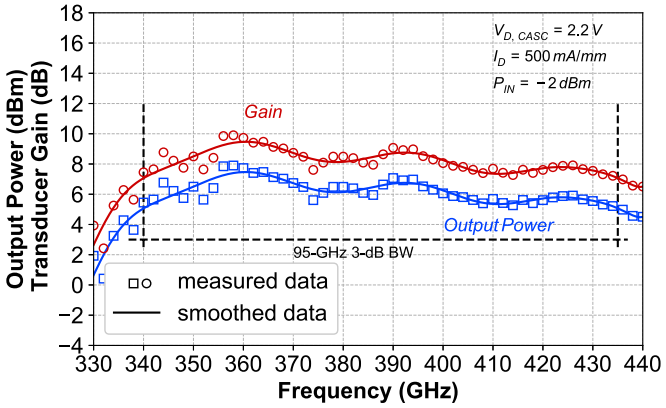

Fig. 9. On-wafer performance of the transmitter with regard to the output power and transducer gain, without the on-chip antenna.

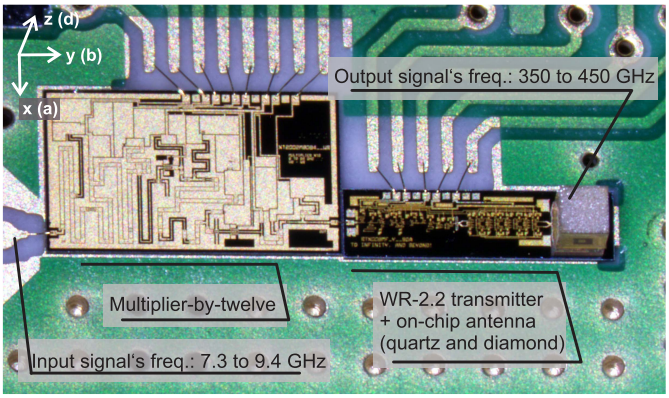

Fig. 10. Photograph of the assembled transmitter chip and multiplier-by-12 on a carrier board.

into a transmitter S-MMIC, as shown in Fig. 8. The analysis of the transmitter-S-MMIC active chain is presented in [31]. It is composed of a multiplier-by-four (×4)—upconverting the input signal from the WR-10 (75–110 GHz) to the WR-2.2 frequency band—and a subsequent high power amplifier (PA) [31]. The corresponding on-wafer characterization is shown in Fig. 9. The output power and transducer gain of the stand-alone active chain is plotted across the measurement frequency range from 330 to 440 GHz. A peak output power and peak transducer gain of 8 dBm and 10 dB are recorded, respectively. A 3 dB bandwidth of 95 GHz spans from 340 to 435 GHz. The output power and gain curves are flat across the operating bandwidth. A relative bandwidth of 24.5% is achieved. The transmitter S-MMIC is assembled on a carrier board, which includes an accompanying in-house multiplier-by-12 [50], as shown in Fig. 10. This setup no longer requires an RF-probe. A baseband signal is fed to the carrier board. This baseband input signal's frequency ranges from 7.3 to 9.4 GHz, the combined 48th harmonic of which enables the acquisition of the far-field patterns from 350 to 450 GHz.

The complete measurement setup can be viewed in Fig. 11, in which the polypropylene-based dielectric lens is included in the antenna-carrier board setup. The device under test is mounted on a KUKA KR 10 R1100 six-axis maneuverable robotic arm. The transmitter is characterized via a WR-2.2 ZRX500 receiver by Radiometer Physics GmbH (RPG) and a respective WR-2.2 horn antenna with 23 dB of gain (also by RPG). The rest of the setup includes two signal sources for the transmitter and receiver, dc-bias power supplies, and a spectrum analyzer.

The far-field patterns are acquired at a distance of 90 mm to the receiver. The transmitter board is tilted in an angle range from −45° to 45° for both the pitch and yaw—along the respective axes and with regard to a fixed phase center—as highlighted in Fig. 11. The measured data, with and without the utilization of a dielectric lens, are plotted in Fig. 12. The principal planes are indicated via the Phi (ϕ) and Theta (θ) angles. The plotted data correspond to $\phi = 90°$—for the electric-field plane (E-plane)—and $\phi = 0°$—for the magnetic-field plane (H-plane). θ is swept across

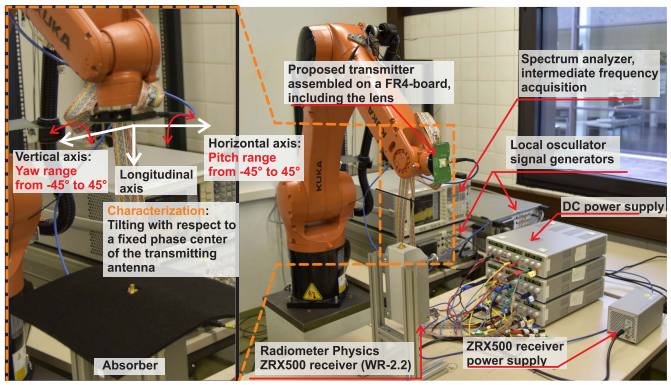

Fig. 11. Far-field pattern characterization setup.

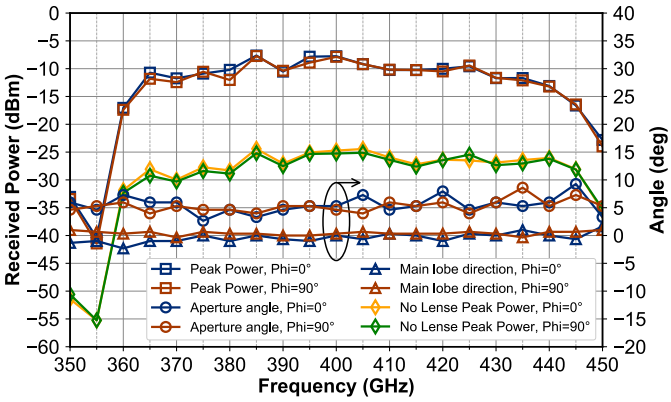

Fig. 12. Received peak power, as well as main-lobe direction, and angular width. The path loss is included. The distance to the receiver is 90 mm.

the pitch- and yaw-angle range. The conversion gain of the receiver is compensated according to the data supplied by the manufacturer. The path loss is included in the plotted data. A 3 dB pattern bandwidth spanning from 365 to 440 GHz can be deduced. The received power ranges from −12 to −9 dBm. Without the lens, the received power spans from −29 to −26 dBm. The resulting difference of 17 dB is attributed to the lens, which collimates the antenna beam. It is dependent on the corresponding aperture illumination, which is affected by the radiation characteristics of the on-chip antenna across the operating bandwidth.

The flat response of the received power is in part due to the performance of the active chain, yet most significantly, it is affected by the operating region of the metastructured ground plane. This is visible in the measured curves, as the drop-off in the received signal coincides with the frequency points where the metastructured layer no longer serves its purpose. However, the sharp drop-off in the lower 3 dB cutoff point is purely affected by the utilized multiplier-by-12 chip. The latter is only able to provide a sufficient 12th-harmonic drive for the frequency range from 90 to 112.5 GHz—beyond which the signal is barely strong enough for the pattern shape to be captured. The truncation of the bandwidth, initially reported in [50], is due to the added bondwires and run-to-run statistical variations in the processing of the wafers. Included in Fig. 12 are the 3 dB main-lobe angular width and the main-lobe direction—for the with-lens case. These are consistent over the operating bandwidth and result in a broadside radiating on-chip antenna with an angular width of 7°.

The measured and normalized far-field patterns, for the with-lens case, in both $\phi = 0°$ (H-plane) and $\phi = 90°$ (E-plane) are presented in Fig. 13(a), over a bandwidth from 350 to 450 GHz. θ ranges from $-45°$ to 45°, limited by the measurement setup. As intended in the design, the patterns are consistent over the measured bandwidth—meaning that they hold the same main-lobe direction throughout. A sidelobe level (SLL) suppression of 10 dB or better is present for each instance of frequency measured. The simulated far-field patterns are included as well. The coherence of the measurement to the simulation—in terms of the angular width, main-lobe direction, and SLL—supports the functionality of the proposed antenna setup.

The measured and normalized far-field patterns for the without-lens case are plotted in Fig. 13(b). Similar to the with-lens case, the measurements span a bandwidth from 350 to 450 GHz. The patterns are consistent throughout the operating bandwidth, with regard to the main-lobe direction and SLL. The angular width is in the range of 50°. Different from the with-lens case, the angular width drifts from 45° to 55° across the operating bandwidth. With the increase in frequency, the angular width decreases. This represents a behavior common to dielectric-resonator-based approaches, as over the complete bandwidth various modes overlap. The ripple on the measurements is due to the accuracy limitations of the spectrum analyzer.

In terms of the simulation, included in Fig. 13(b), the overlap with the measurement is satisfactory. This is the case for all frequency points, namely, 350, 370, 400, and 430 GHz—except for the case of 450 GHz, where the 3-D EM model deviates in terms of the SLL. The later becomes apparent when the lens is absent. To be noted is that a complete one-to-one overlap is highly unlikely for the operating frequencies at hand. This is due to the challenges in creating a 3-D EM model that completely mimics the processed BEOL structuring (systematic deviations from design sizes). Furthermore, the expected load targets dependent on the biasing of the active chain (meaning the output impedance that is presented to the input of the antenna), the variations in quartz and diamond placement, as well as the submount-carrier-board deviations in terms of the lens positioning (since the latter attaches to the former) are all factors that present a great difficulty when attempting an inclusion in a 3-D EM simulation.

In order to derive the directivity from the presented data, a clear understanding of each component in the measurement setup needs to be obtained. The known quantities include the on-wafer performance of the active-transmitter chain, the difference in the received power due to the lens, the standard-gain horn, the conversion gain of the receiver, and the distance to it. The contemporary interpretation of Friis' transmission formula, originally presented in [51], is utilized to derive the antenna directivity from the measurements

$$\begin{aligned} P_{\mathrm{R}} &= P_{\mathrm{T}} + D_{\mathrm{T}} + D_{\mathrm{R}} + 10\log_{10}\left(\frac{\lambda}{4\pi d}\right)^2 \\ &= P_{\mathrm{T}} + (\Delta G_{\mathrm{lens}} + D_{\mathrm{ant.}}) + (D_{\mathrm{horn}} + \mathrm{CG}_{\mathrm{ZRX500}}) \\ &\quad + 20\log_{10}\left(\frac{\lambda}{4\pi d}\right). \end{aligned} \tag{28}$$

P_{R} denotes the received power at the output terminal of the respective antenna, in this case the received power seen in Fig. 12. P_{T} is the power fed into the transmitting-antenna input port, in this case the on-wafer measured output power of the active-transmitter chain presented in Fig. 9. The directivity of the transmitting device is labeled D_{T}. In this case, it is composed of the contribution via collimation by the lens ΔG_{lens} and the directivity of the on-chip antenna $D_{\mathrm{ant.}}$. The former can be extracted from Fig. 12. The latter is the desired unknown. The wavelength and distance between the transmitting and receiving antenna are represented by λ and d, respectively.

The plot of the directivity and antenna efficiency is presented in Fig. 14. With regard to the directivity, a good coherence between the measurement and simulation is present. Both align to a large degree over the complete operating bandwidth, which is truncated in the upper frequency band due to the active chain only having undergone large-signal characterization up to 440 GHz. As a consequence, a P_{T} reference is absent for the frequencies beyond. Considering the received power in Fig. 12, the directivity extracted from the measurements ranges from 4.4 to 10.4 dBi. It satisfies the simulated variant of 6 to 10 dBi. Including the lens, it spans from 22 to 27 dBi. The difference is dependent on the aperture illumination of the lens. Since the on-chip antenna angular width varies across the operating bandwidth, so does the degree of illumination of the aperture—thus the effectiveness of the lens across bandwidth. The EIRP is plotted as well, and it ranges from 27.5 to 32.9 dBm. It is calculated via the summation of P_{T}, $D_{\mathrm{ant.}}$, and ΔG_{lens}.

The plotted efficiency is that of the simulation since measuring a radiation efficiency is impossible in the proposed setup. First, the antenna load pulling on the output of the active chain, when operated under large-signal driving conditions, is in this current arrangement not characterizable. The on-wafer characterization of the said chip, when the output is terminated with the on-chip antenna rather than an electrically short RF-pad, is not reliable. This is due to the presence of the on-chip antenna resonance within the output characteristics of the active chain since it is seen in parallel to the RF-contacting probes. Another aspect is the effective bias condition observed

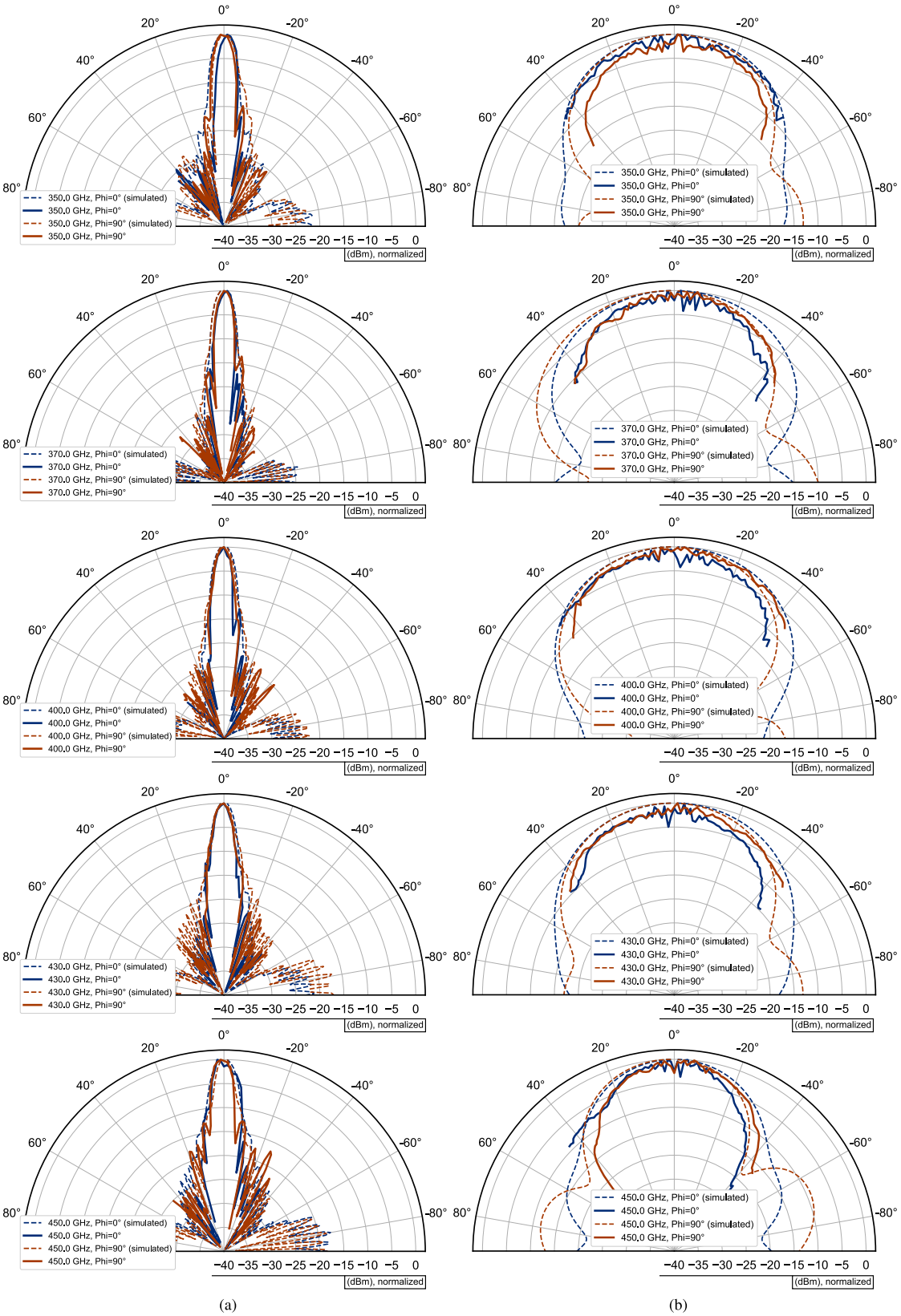

Fig. 13. Measured versus simulated far-field patterns, both normalized, over a frequency range from 350 to 450 GHz, for (a) with-lens and (b) without-lens case.

during the on-wafer characterization, which cannot be one-to-one replicated in the far-field measurements. This is due to the presence of a biasing board and discrete power supplies, instead of a source and measure unit. Furthermore, the active chain of the chip is characterized via direct probing, different from the final setup, where the submount contains a

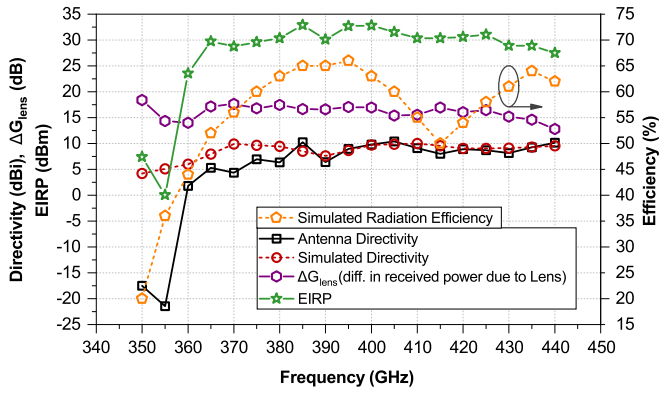

Fig. 14. Antenna directivity, efficiency, and EIRP.

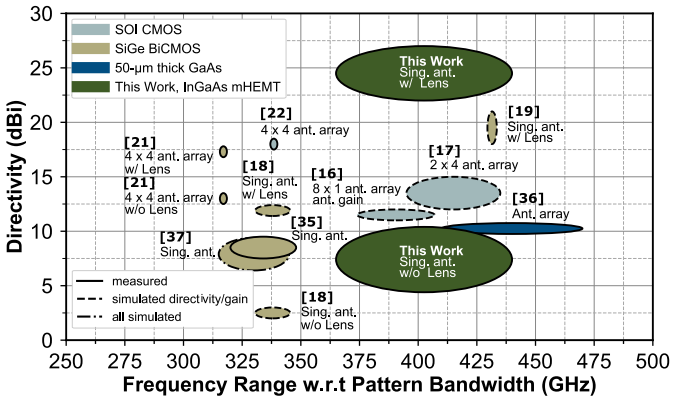

Fig. 15. Directivity versus frequency range with respect to the pattern bandwidth for on-chip antenna solutions operating in the frequency range from 300 to 500 GHz. The directivity is encoded in the minor axes of the ellipses and the pattern bandwidth in the major axes.

multiplier-by-12 up front. Directly probing the antenna is not a solution either since the RF-probe is always within the near field of it. The absence of a reference measurement is also significant, as this is an integrated antenna solution rather than a waveguide split-block-module-based one. The latter may be mounted on a reference setup, calibrated with known standard-gain horn antennas.

Considering the characterization difficulties listed above and the effectiveness of the simulation model with regard to the far-field patterns, S_{11}, and the directivity, it is reasonable to assume that the radiation efficiency will be comparable to the simulation plotted in Fig. 14—within a reasoning framework that considers a certain degree of simulation uncertainty. Within the operating bandwidth, the simulated efficiency varies from 50% to 66%. Despite the suboptimal substrate height, through the utilization of the metastructured ground plane, it is possible to achieve efficiencies commonly expected from patch-antenna-based implementation with a closer-to-ideal substrate thickness.

A comparison of the most significant and recently published results for on-chip antenna solutions operating in the frequency range from 300 to 500 GHz is presented in Fig. 15, in which the directivity is plotted across the pattern bandwidth. Both parameters are depicted via an elliptical shape, with the directivity encoded on the minor axis, while the bandwidth is encoded on the major axis. The included on-chip antenna examples contain arrays, as well as singular elements, with and without the implementation of a dielectric lens. Both to-the-broadside and through-the-substrate radiating concepts are considered. Whether the provided information is measured or simulated, can be deduced by the type of line composing the circumference of the ellipses.

With regard to the measured pattern bandwidth, the proposed solution sets the state-of-the-art spanning from 365 to 440 GHz. This constitutes a relative pattern bandwidth of 19.6%. With regard to the measured directivity, the achieved peak value of 10.4 dBi, without the lens, is comparable to array-based solutions presented in [36] and [16] and singular antenna implementations reported in [35] and [23]. In combination with the utilized dielectric lens, the achieved value of 27 dBi sets the absolute state of the art.

V. Conclusion

This article presents the analysis, modeling, design, simulation, and characterization of a novel combination between a metastructured ground plane, a microstrip patch, a quartz-based dielectric resonator, and a diamond-based antireflex layer to realize an efficient, broadband, and to-the-broadside radiating 400 GHz on-chip antenna in a 35 nm InGaAs mHEMT process. The proposed solution represents a first-time implementation for all submillimeter-wave-capable semiconductor technologies. It achieves a measured impedance bandwidth of 100 GHz, a pattern bandwidth of 75 GHz, an efficiency of 50%–66%, and a directivity of up to 27 dBi—with the utilization of a polypropylene-based dielectric lens.

Implemented in the selected semiconductor technology, any to-the-broadside radiating on-chip antenna concept has to overcome a substrate-thickness limitation of 4.98 μm, which favors a leaky capacitor instead of broadband antenna. To solve the said issue, a metastructured ground plane is implemented that reflects the substrate-incident waves with a desired phase delay, ensuring that the reflected and the radiated waves undergo constructive interference. An analysis on the design of the metastructure is presented, as well as two modeling approaches are revealed and compared. Between the analytical and 3-D EM model, the latter is selected as it allows for the inclusion of the microstrip patch, the dielectric resonator, the antireflex layer, and the lens. While the metastructure improves the efficiency and impedance bandwidth, the coapplication in-tandem with a quartz-based dielectric resonator allows for the generation of consistent far-field patterns via the superposition of multiple modes across the operating bandwidth. The utilization of a diamond-based antireflex layer aids in the decoupling of the EM waves from the quartz to free space.

Due to the minuscule size of the proposed antenna concept, the only means of far-field characterization, where no RF-probe is within the near field, is through the integration into a complete transmitter S-MMIC—750 $\times$ 2750 μm^2 in size. The said chip is placed on a carrier board, upon which the respective polypropylene-based dielectric lens is mounted.

The pattern characterization is performed with the aid of a maneuverable robotic arm. Simulation and measurement results of both with and without the lens are shown, and a good agreement between theoretical and experimental data is observed.

ACKNOWLEDGMENT

The authors would like to acknowledge and thank their colleagues at the Fraunhofer Institute for Applied Solid State Physics (IAF), Freiburg im Breisgau, Germany: Oliver Göhlich for his excellent work in coat-spinning and positioning of the quartz dielectric resonators, Birgit Weismann-Thaden for dicing the quartz wafers, Ralf Schmidt and Martin Zink for laser cutting the diamond plates, and Dirk Meder for assembling the evaluation boards.

REFERENCES

[1] R. Piesiewicz *et al.*, "Short-range ultra-broadband terahertz communications: Concepts and perspectives," *IEEE Antennas Propag. Mag.*, vol. 49, no. 6, pp. 24–39, Dec. 2007, doi: 10.1109/MAP.2007.4455844.

[2] H.-J. Song and T. Nagatsuma, "Present and future of terahertz communications," *IEEE Trans. THz Sci. Technol.*, vol. 1, no. 1, pp. 256–263, Sep. 2011, doi: 10.1109/TTHZ.2011.2159552.

[3] J. Antes and I. Kallfass, "Performance estimation for broadband multi-gigabit millimeter- and sub-millimeter-wave wireless communication links," *IEEE Trans. Microw. Theory Techn.*, vol. 63, no. 10, pp. 3288–3299, Oct. 2015, doi: 10.1109/TMTT.2015.2467390.

[4] C. Castro, R. Elschner, T. Merkle, C. Schubert, and R. Freund, "Long-range high-speed THz-wireless transmission in the 300 GHz band," in *Proc. 3rd Int. Workshop Mobile THz Syst. (IWMTS)*, Jul. 2020, pp. 1–4, doi: 10.1109/IWMTS49292.2020.9166263.

[5] G. Ducournau *et al.*, "Ultrawide-bandwidth single-channel 0.4-THz wireless link combining broadband quasi-optic photomixer and coherent detection," *IEEE Trans. THz Sci. Technol.*, vol. 4, no. 3, pp. 328–337, May 2014, doi: 10.1109/TTHZ.2014.2309006.

[6] H.-B. Liu, H. Zhong, N. Karpowicz, Y. Chen, and X.-C. Zhang, "Terahertz spectroscopy and imaging for defense and security applications," *Proc. IEEE*, vol. 95, no. 8, pp. 1514–1527, Aug. 2007, doi: 10.1109/JPROC.2007.898903.

[7] F. Friederich *et al.*, "THz active imaging systems with real-time capabilities," *IEEE Trans. THz Sci. Techn.*, vol. 1, no. 1, pp. 183–200, Aug. 2011, doi: 10.1109/TTHZ.2011.2159559.

[8] K. B. Cooper and G. Chattopadhyay, "Submillimeter-wave radar: Solid-state system design and applications," *IEEE Microw. Mag.*, vol. 15, no. 7, pp. 51–67, Nov. 2014, doi: 10.1109/MMM.2014.2356092.

[9] P. Lopato, "Double-sided terahertz imaging of multilayered glass fiber-reinforced polymer," *Appl. Sci.*, vol. 7, no. 7, p. 661, Jun. 2017, doi: 10.3390/app7070661.

[10] D. Meier *et al.*, "Propagation of millimeter waves in composite materials," *IEEE Trans. Antennas Propag.*, vol. 68, no. 4, pp. 3080–3093, Apr. 2020, doi: 10.1109/TAP.2019.2955213.

[11] M. Caris, S. Stanko, S. Palm, R. Sommer, A. Wahlen, and N. Pohl, "300 GHz radar for high resolution SAR and ISAR applications," in *Proc. 16th Int. Radar Symp. (IRS)*, Jun. 2015, pp. 577–580, doi: 10.1109/IRS.2015.7226313.

[12] D. Meier *et al.*, "Millimeter-wave tomographic imaging of composite materials based on phase evaluation," *IEEE Trans. Microw. Theory Techn.*, vol. 67, no. 10, pp. 4055–4068, Oct. 2019, doi: 10.1109/TMTT.2019.2929153.

[13] S. Stanko, S. Palm, R. Sommer, F. Kloppel, M. Caris, and N. Pohl, "Millimeter resolution SAR imaging of infrastructure in the lower THz region using MIRANDA-300," in *Proc. 46th Eur. Microw. Conf. (EuMC)*, Oct. 2016, pp. 1505–1508, doi: 10.1109/EuMC.2016.7824641.

[14] T. Jaeschke, C. Bredendiek, and N. Pohl, "A 240 GHz ultra-wideband FMCW radar system with on-chip antennas for high resolution radar imaging," in *IEEE MTT-S Int. Microw. Symp. Dig.*, Jun. 2013, pp. 1–4, doi: 10.1109/MWSYM.2013.6697495.

[15] K. B. Cooper, R. J. Dengler, N. Llombart, B. Thomas, G. Chattopadhyay, and P. H. Siegel, "THz imaging radar for standoff personnel screening," *IEEE Trans. THz Sci. Technol.*, vol. 1, no. 1, pp. 169–182, Sep. 2011, doi: 10.1109/TTHZ.2011.2159556.

[16] Y. Yang, O. D. Gurbuz, and G. M. Rebeiz, "An eight-element 370–410-GHz phased-array transmitter in 45-nm CMOS SOI with peak EIRP of 8–8.5 dBm," *IEEE Trans. Microw. Theory Techn.*, vol. 64, no. 12, pp. 4241–4249, Dec. 2016, doi: 10.1109/TMTT.2016.2613850.

[17] F. Golcuk, O. D. Gurbuz, and G. M. Rebeiz, "A 0.39–0.44 THz 2×4 amplifier-quadrupler array with peak EIRP of 3–4 dBm," *IEEE Trans. Microw. Theory Techn.*, vol. 61, no. 12, pp. 4483–4491, Dec. 2013, doi: 10.1109/TMTT.2013.2287493.

[18] J. Al-Eryani, H. Knapp, J. Kammerer, K. Aufinger, H. Li, and L. Maurer, "Fully integrated single-chip 305–375-GHz transceiver with on-chip antennas in SiGe BiCMOS," *IEEE Trans. THz Sci. Technol.*, vol. 8, no. 3, pp. 329–339, May 2018, doi: 10.1109/TTHZ.2018.2823202.

[19] P. Hillger, J. Grzyb, S. Malz, B. Heinemann, and U. Pfeiffer, "A lens-integrated 430 GHz SiGe HBT source with up to −6.3 dBm radiated power," in *Proc. IEEE Radio Freq. Integr. Circuits Symp. (RFIC)*, Jun. 2017, pp. 160–163, doi: 10.1109/RFIC.2017.7969042.

[20] P. Hillger, J. Grzyb, R. Lachner, and U. Pfeiffer, "An antenna-coupled 0.49 THz SiGe HBT source for active illumination in terahertz imaging applications," in *Proc. 10th Eur. Microw. Integr. Circuits Conf. (EuMIC)*, Sep. 2015, pp. 180–183, doi: 10.1109/EuMIC.2015.7345098.

[21] R. Han *et al.*, "A SiGe terahertz heterodyne imaging transmitter with 3.3 mW radiated power and fully-integrated phase-locked loop," *IEEE J. Solid-State Circuits*, vol. 50, no. 12, pp. 2935–2947, Dec. 2015, doi: 10.1109/JSSC.2015.2471847.

[22] Y. Tousi and E. Afshari, "A high-power and scalable 2-D phased array for terahertz CMOS integrated systems," *IEEE J. Solid-State Circuits*, vol. 50, no. 2, pp. 597–609, Feb. 2015, doi: 10.1109/JSSC.2014.2375324.

[23] C.-H. Li, C.-L. Ko, M.-C. Kuo, and D.-C. Chang, "A 340-GHz heterodyne receiver front end in 40-nm CMOS for THz biomedical imaging applications," *IEEE Trans. THz Sci. Technol.*, vol. 6, no. 4, pp. 625–636, Jul. 2016, doi: 10.1109/TTHZ.2016.2566580.

[24] B. Khamaisi and E. Socher, "130–320-GHz CMOS harmonic down-converters around and above the cutoff frequency," *IEEE Trans. Microw. Theory Techn.*, vol. 63, no. 7, pp. 2275–2288, Jul. 2015, doi: 10.1109/TMTT.2015.2431671.

[25] Y.-J. Chen and T.-S. Chu, "A 312-GHz antenna array receiver in 65 nm CMOS utilizing self-oscillating 3X subharmonic mixer frontend," in *Proc. IEEE Radio Freq. Integr. Circuits Symp. (RFIC)*, May 2015, pp. 19–22, doi: 10.1109/RFIC.2015.7337694.

[26] L. Wu, S. Liao, and Q. Xue, "A 312-GHz CMOS injection-locked radiator with chip-and-package distributed antenna," *IEEE J. Solid-State Circuits*, vol. 52, no. 11, pp. 2920–2933, Nov. 2017, doi: 10.1109/JSSC.2017.2727046.

[27] P. Hillger, J. Grzyb, R. Jain, and U. R. Pfeiffer, "Terahertz imaging and sensing applications with silicon-based technologies," *IEEE Trans. THz Sci. Technol.*, vol. 9, no. 1, pp. 1–19, Jan. 2019, doi: 10.1109/TTHZ.2018.2884852.

[28] A. Leuther *et al.*, "35-nm metamorphic HEMT MMIC technology," in *Proc. 20th Int. Conf. Indium Phosph. Rel. Mater.*, May 2008, pp. 1–4, doi: 10.1109/ICIPRM.2008.4702910.

[29] A. Leuther, T. Merkle, R. Weber, R. Sommer, and A. Tessmann, "THz frequency HEMTs: Future trends and applications," in *Proc. Compound Semicond. Week (CSW)*, May 2019, pp. 1–2, doi: 10.1109/ICIPRM.2019.8819000.

[30] B. Gashi *et al.*, "Broadband and high-gain 400-GHz InGaAs mHEMT medium-power amplifier S-MMIC," in *IEEE MTT-S Int. Microw. Symp. Dig.*, Aug. 2020, pp. 484–487, doi: 10.1109/IMS30576.2020.9223968.

[31] B. Gashi *et al.*, "Broadband 400-GHz InGaAs mHEMT transmitter and receiver S-MMICs," *IEEE Trans. THz Sci. Technol.*, vol. 11, no. 6, pp. 660–675, Nov. 2021, doi: 10.1109/TTHZ.2021.3099064.

[32] L. John *et al.*, "A 280–310 GHz InAlAs/InGaAs mHEMT power amplifier MMIC with 6.7–8.3 dBm output power," *IEEE Microw. Wireless Compon. Lett.*, vol. 29, no. 2, pp. 143–145, Feb. 2019, doi: 10.1109/LMWC.2018.2885916.

[33] F. Thome and A. Leuther, "A 75–305-GHz power amplifier MMIC with 10–14.9-dBm P_{out} in a 35-nm InGaAs mHEMT technology," *IEEE Microw. Wireless Compon. Lett.*, vol. 31, no. 6, pp. 741–743, Jun. 2021, doi: 10.1109/LMWC.2021.3058101.

[34] L. Shafai, P. Mousavi, and R. Mirzavand, "Wideband microstrip antennas," in *Antenna Engineering Handbook*, 5th ed., J. L. Volakis, Ed. New York, NY, USA: McGraw-Hill, 2018, ch. 9, pp. 198–200. [Online]. Available: https://www.accessengineeringlibrary.com/content/book/9781259644696

[35] X.-D. Deng, Y. Li, C. Liu, W. Wu, and Y.-Z. Xiong, "340 GHz on-chip 3-D antenna with 10 dBi gain and 80% radiation efficiency," *IEEE Trans. THz Sci. Technol.*, vol. 5, no. 4, pp. 619–627, Jul. 2015, doi: 10.1109/TTHZ.2015.2424682.
[36] M. Alibakhshikenari *et al.*, "Study on improvement of the performance parameters of a novel 0.41–0.47 THz on-chip antenna based on metasurface concept realized on 50 μm GaAs-layer," *Sci. Rep.*, vol. 10, no. 1, Dec. 2020, Art. no. 11034, doi: 10.1038/s41598-020-68105-z.
[37] C.-H. Li and T.-Y. Chiu, "340-GHz low-cost and high-gain on-chip higher order mode dielectric resonator antenna for THZ applications," *IEEE Trans. THz Sci. Technol.*, vol. 7, no. 3, pp. 284–294, May 2017, doi: 10.1109/TTHZ.2017.2670234.
[38] M. Alibakhshikenari, B. S. Virdee, C. H. See, R. A. Abd-Alhameed, F. Falcone, and E. Limiti, "Overcome the limitations of performance parameters of on-chip antennas based on metasurface and coupled feeding approaches for applications in system-on-chip for THz integrated-circuits," in *Proc. IEEE Asia–Pacific Microw. Conf. (APMC)*, Dec. 2019, pp. 246–248, doi: 10.1109/APMC46564.2019.9038524.
[39] M. N. Afsar, "Precision millimeter-wave measurements of complex refractive index, complex dielectric permittivity, and loss tangent of common polymers," *IEEE Trans. Instrum. Meas.*, vol. IM-36, no. 2, pp. 530–536, Jun. 1987, doi: 10.1109/TIM.1987.6312733.
[40] D. Sievenpiper, L. Zhang, R. F. J. Broas, N. G. Alexopolous, and E. Yablonovitch, "High-impedance electromagnetic surfaces with a forbidden frequency band," *IEEE Trans. Microw. Theory Techn.*, vol. 47, no. 11, pp. 2059–2074, Nov. 1999, doi: 10.1109/22.798001.
[41] D. F. Sievenpiper, "High-impedance electromagnetic surfaces," Ph.D. dissertation, Dept. Elect. Eng. Comput. Sci., Univ. California, Los Angeles, CA, USA, 1999. [Online]. Available: http://optoelectronics.eecs.berkeley.edu/ThesisDan.pdf
[42] F. Yang and Y. Rahmat-Samii, *Electromagnetic Band Gap Structures in Antenna Engineering* (The Cambridge RF and Microwave Engineering Series). Cambridge, U.K.: Cambridge, Univ. Press, 2009, doi: 10.1017/CBO9780511754531.
[43] C. R. Simovski, P. De Maagt, and I. V. Melchakova, "High-impedance surfaces having stable resonance with respect to polarization and incidence angle," *IEEE Trans. Antennas Propag.*, vol. 53, no. 3, pp. 908–914, Mar. 2005, doi: 10.1109/TAP.2004.842598.
[44] S. Maci, M. Caiazzo, A. Cucini, and M. Casaletti, "A pole-zero matching method for EBG surfaces composed of a dipole FSS printed on a grounded dielectric slab," *IEEE Trans. Antennas Propag.*, vol. 53, no. 1, pp. 70–81, Jan. 2005, doi: 10.1109/TAP.2004.840520.
[45] C. Balanis, *Antenna Theory: Analysis and Design*, 4th ed., Hoboken, NJ, USA: Wiley, 2015. [Online]. Available: https://www.wiley.com/-p-9781119178996
[46] R. Yaduvanshi and H. Parthasarathy, *Rectangular Dielectric Resonator Antenna: Theory and Design*. New Delhi, India: Springer, 2016, doi: 10.1007/978-81-322-2500-3.
[47] T. A. Milligan, *Modern Antenna Design* (IEEE Press), 2nd ed. Hoboken, NJ, USA: Wiley, 2005, doi: 10.1002/0471720615.
[48] R. Munson, "Conformal microstrip antennas and microstrip phased arrays," *IEEE Trans. Antennas Propag.*, vol. AP-22, no. 1, pp. 74–78, Jan. 1974, doi: 10.1109/TAP.1974.1140723.
[49] M. V. Schneider, "Microstrip lines for microwave integrated circuits," *Bell Syst. Tech. J.*, vol. 48, no. 5, pp. 1421–1444, May/Jun. 1969, doi: 10.1002/j.1538-7305.1969.tb04274.x.
[50] R. Weber, U. Lewark, A. Leuther, and I. Kallfass, "A W-band $\times 12$ multiplier MMIC with excellent spurious suppression," *IEEE Microw. Wireless Compon. Lett.*, vol. 21, no. 4, pp. 212–214, Mar. 2011, doi: 10.1109/LMWC.2011.2106486.
[51] H. T. Friis, "A note on a simple transmission formula," *Proc. IRE*, vol. 34, no. 5, pp. 254–256, May 1946, doi: 10.1109/JRPROC.1946.234568.

Bersant Gashi received the M.Sc. degree in embedded systems engineering from the University of Freiburg, Freiburg im Breisgau, Germany, in 2018, where he is currently pursuing the Dr.Ing. degree.

In June 2017, he joined the Fraunhofer Institute for Applied Solid State Physics (IAF), Freiburg im Breisgau. His current research interests are in the field of submillimeter-wave MMICs and broadband antennas for modern radar and communication applications.

Dominik Meier received the M.Sc. degree in electrical engineering from the Karlsruhe Institute of Technology (KIT), Karlsruhe, Germany, in 2013, and the Ph.D. degree from the University of Freiburg, Freiburg im Breisgau, Germany, in 2021.

From 2013 to 2015, he worked as a Research Assistant with the University of Stuttgart, Stuttgart, Germany. From 2015 to 2021, he was with the Department of Microelectronics, Fraunhofer Institute for Applied Solid State Physics (IAF), Freiburg im Breisgau. At the IAF, his research interests included the millimeter-wave characterization of composite materials, millimeter-wave radar systems, and signal analysis. Since 2021, he has been with AP Sensing GmbH, Böblingen, Germany.

Laurenz John received the M.Sc. and Ph.D. (Dr.Ing.) degrees in electrical engineering and information technologies from the Karlsruhe Institute of Technology (KIT), Karlsruhe, Germany, in 2016 and 2021, respectively.

He is currently an RF Design Engineer and a Project Leader with the Fraunhofer Institute for Applied Solid State Physics (IAF), Freiburg im Breisgau, Germany. Since 2016, he has been involved in the design and characterization of InGaAs-channel HEMT devices and integrated circuits on GaAs and Si substrates for mm-wave and sub-mm-wave frequency applications up to 800 GHz. His current research interests include integrated circuit (IC) and package design for radar, communication, and quantum computing applications at millimeter-wave and terahertz frequencies.

Benjamin Baumann received the B.Eng. degree from the Baden-Wuerttemberg Cooperative State University Loerrach (DHBW-Loerrach), Loerrach, Germany, in 2013, and the M.Sc. degree in electrical engineering and information technology from the University of Duisburg-Essen, Duisburg, Germany, in 2019.

Since 2013, he has been a Research Engineer with the Department of Microelectronics, Fraunhofer Institute for Applied Solid State Physics (IAF), Freiburg im Breisgau, Germany. His scientific interests include millimeter-wave radar systems, phase-locked loop-based signal generators, the design and characterization of millimeter-wave antennas, and mixed-signal printed circuit boards.

Markus Rösch received the Dipl.-Ing. degree in electrical engineering and the Dr.Ing. degree from the Karlsruhe Institute of Technology (KIT), Karlsruhe, Germany, in 2008 and 2013, respectively.

From November 2008 to June 2012, he was a Ph.D. Student with the Institut de Radioastronomie Millimétrique (IRAM), St. Martin d'Hères, France, where he developed superconducting kinetic inductance detectors (KID) for millimeter-wave astronomy. From 2012 to 2021, he was a Research Engineer with the Fraunhofer Institute for Applied Solid State Physics (IAF), Freiburg im Breisgau, Germany, where he led the systems group from 2018 to 2021. Since 2021, he has been with Dolphin Design SAS, Meylan, France. His research topics include radar sensors and systems for millimeter-wave technologies.

Axel Tessmann received the Dipl.-Ing. and Ph.D. degrees in electrical engineering from the University of Karlsruhe, Karlsruhe, Germany, in 1997 and 2006, respectively.

In 1997, he joined the Department of Microelectronics, Fraunhofer Institute for Applied Solid State Physics (IAF), Freiburg im Breisgau, Germany, where he is involved in the development of monolithically integrated circuits and subsystems for high-resolution imaging systems and high data rate wireless communication links. He is currently a Group Manager with the Millimeter-Wave Packaging and Subsystem Group, Fraunhofer IAF. His main research areas are the design and packaging of millimeter-wave and submillimeter-wave ICs using high-electron-mobility transistors on GaAs, GaN, and InP as well as circuit simulation, and linear and nonlinear device modeling.

Arnulf Leuther received the Dipl. Phys. and Ph.D. degrees in physics from the Technical University of Aachen, Aachen, Germany, in 1992 and 1996, respectively.

Since 1996, he has been with the Fraunhofer Institute for Applied Solid State Physics (IAF), Freiburg im Breisgau, Germany. His research interests include the development of high-electron-mobility transistor technologies for sensor and communication systems up to 800 GHz.

Rüdiger Quay (Senior Member, IEEE) received the Diploma degree in physics from Rheinisch-Westfälische Technische Hochschule (RWTH), Aachen, Germany, in 1997, and the Ph.D. degree (Hons.) in technical sciences, the second Diploma degree in economics, and the Venia Legendi (Habilitation) degree in microelectronics from the Technische Universität Vienna, Vienna, Austria, in 2001, 2003, and 2009, respectively.

In 2001, he joined the Fraunhofer Institute for Applied Solid-State Physics, Freiburg im Breisgau, Germany, where he currently serves as the Executive Director. Since 2020, he holds the Fritz-Hüttinger Endowed Chair in energy-efficient high-frequency electronics with the Institute for Sustainable System Engineering, University of Freiburg, Freiburg im Breisgau. He authored and coauthored 300 refereed publications, three monographs, and made contributions to further two.